Harnessing hyperspectral imagery to map surface water presence and hyporheic flow properties of headwater stream networks

D. N. Dralle [1], D. A. Lapides [1,2] , D. M. Rempe [3] , W. J. Hahm [2]

[1] United States Forest Service Pacific Southwest Research Station, Davis, CA, USA

[2] Department of Geography, Simon Fraser University, Burnaby, BC, Canada

[3] Department of Geological Sciences, University of Texas-Austin, Austin, TX, USA

Harnessing hyperspectral imagery to map surface water presence and hyporheic flow properties of headwater stream networks

D.N. Dralle[1], D.A. Lapides[1,2], D.M. Rempe[3], W.J. Hahm[2],

[1]Pacific Southwest Research Station, United States Forest Service, Davis, CA, USA
[2]Simon Fraser University, Burnaby, BC, Canada [3]University of Texas at Austin, Austin, TX, USA

Key Points:

- Wetted channels are mapped with 91% accuracy using machine learning and high spatio-temporal resolution hyperspectral imagery.
- Coincident observations of runoff and wetted channels enable estimation of hydraulic properties of the hyporheic zone.
- The scaling of hyporheic properties with contributing area exhibits punctuated break points explained by stream network topology.

Corresponding author: D.N. Dralle, `david.dralle@usda.gov`

Abstract

Growth and contraction of headwater stream networks determine the extent and quality of ecologically critical habitat, and open a window into the storage dynamics of catchments. A fundamental challenge is observation of the process itself: wetted channel extent is highly dynamic in space and time, with the length of wetted channel sometimes varying by orders of magnitude over the course of a single storm event in headwater catchments. To date, observational datasets are largely limited to laborious boots-on-the-ground campaigns, drone imaging, or flow presence sensors, which are limited in their spatial and temporal extents. Here, we evaluate high-resolution, multi-band satellite imagery as a means to detect wetted channel extent via machine learning methods trained using existing wetted channel extent surveys. Even where channel features are smaller than the spatial resolution of the imagery, the absence or presence of surface water may nevertheless be imprinted upon the spectral signature of an individual pixel. We leverage existing wetted channel extent surveys at two oak savanna catchments in northern California with minimal riparian canopy cover and highly dynamic wetted channel extent due to small subsurface water storage capacity and saturation overland flow. We train a random forest model on high-resolution ($\sim$5 m pixel) RapidEye satellite imagery captured contemporaneously with the existing surveys. Withheld test data indicates prediction of wet vs. dry channel extent with >91% accuracy. This predictive ability is used to produce length-discharge (L-Q) relations and to calculate spatially distributed estimates of channel hyporheic flow capacity and exchange. A sharp break in hyporheic flow properties occurs at the transition from main stem channels to lower order tributaries, also resulting in a stepped L-Q relationship that cannot be captured by traditionally used power law models. Remotely sensed imagery is a powerful tool for producing wetted channel maps at high spatial resolution ($\sim$10 m in this study to channels with > 0.01 km^2 contributing area).

1 Introduction

Stream networks expand and contract through time, yielding insight into how hillslope runoff generation interacts with channel hydrogeomorphology to create aquatic ecosystem habitat. Ephemeral and intermittent streams constitute half of Earth's fluvial channel network (Datry et al., 2007; Kampf et al., 2021), and are increasingly being studied due to their role in a wide range of earth system processes (Fovet et al., 2021), such as carbon transport (e.g. Wondzell & Ward, 2022), water transit times (e.g. Lapides et al., 2022), and water-borne disease transmission (e.g. Perez-Saez et al., 2017). Historically, time-consuming walking surveys have provided the observational basis for our understanding of the dynamic extent of wetted stream channels in headwater catchments (e.g. Godsey & Kirchner, 2014; Lovill et al., 2018; Whiting & Godsey, 2016). However, these surveys are limited in their spatiotemporal coverage: less than 0.0001% of Earth's ice-free land area has been repeatedly mapped (Lapides et al., 2021), underscoring the status of headwater stream networks as *aqua incognita* (Bishop et al., 2008). Sparse observations have limited exploration of the physical controls on channel growth and contraction (Moidu et al., 2021).

What determines whether the surface is wetted along a particular reach? In their description of the variable source area concept, Hewlett & Hibbert (1967) noted that:

> "...when the subsurface flow of water from upslope exceeds the capacity of the soil profile to transmit it, the water will come to the surface and channel length will grow."

This flow-emergence principle is applicable on both hillslopes—where saturation overland flow may be generated (Beven & Kirkby, 1979)—as well as in channels—where the presence of water at the surface depends on whether the up-network delivery of water to a point exceeds the subsurface flow capacity of the hyporheic zone (equal to the product of the local slope and cross-sectional area-average conductivity of the bed material in the hyporheic zone). The idea appeared again in the context of network-scale wetted channel extent mapping (Godsey & Kirchner, 2014), re-invigorating the study of process controls on stream network dynamics.

An important implication of the flow-emergence principle is that when a reach transitions from wet to dry, the flow being conveyed by the channel at that point equals the hyporheic flow capacity (Godsey & Kirchner, 2014; Prancevic & Kirchner, 2019; Durighetto et al., 2020). If runoff generation is uniform in space, then area-normalized discharge (Q [L T^{-1}]) at the catchment outlet can be used as an estimate for runoff at any point in the watershed. Thus, instantaneous unit runoff measured at the outlet can be used to approximate hyporheic flow capacity (ρ [L T^{-1}]) at points in the network that are transitioning from wet to dry (Durighetto & Botter, 2022). Because flow capacity varies throughout the network (due to local topographic and hyporheic properties), a range of wetted channel extent maps are required to identify the flow thresholds that delineate wet and dry states throughout the watershed. Paired with the flow-emergence principle and an assumption of spatially uniform unit runoff, surface water presence-absence dynamics provide a unique window into the hyporheic zone, which has generally been difficult to characterize (Ward et al., 2018; Wondzell, 2011).

Establishing a record of wetted channel extent across the full range of observed flows remains a challenging task (Jaeger et al., 2021). Recent methodological developments, such as the deployment of flow presence-absence sensors and drone surveys (e.g. Dugdale et al., 2022; Carbonneau et al., 2020; Zanetti et al., 2022), provide important constraints, but tend to be limited in space or time. Water presence can be detected in large open water (Wang et al., 2022) bodies or main stem river reaches with width greater than existing satellite imagery pixel resolutions (∼10-30 m pixel, Wang et al., 2022; Li et al., 2020; Qin et al., 2021; Verma et al., 2021). However, headwater stream widths are typically less than a couple meters (Allen et al., 2018), much smaller than most satellite data products. But, there is evidence that, even if a channel is smaller than the satellite image pixel scale, individual pixels themselves may contain enough spectral information to indicate when transitions in cover type (e.g. wet to dry, forested to not forested; Chambers et al., 2009; Ling et al., 2020; Carbonneau et al., 2020; Xue et al., 2022). Here, we explore the ability of a random forest machine learning model to identify the presence of wetted channels at the sub-pixel scale with relatively high resolution (5 m pixel) satellite imagery trained on existing wetted channel surveys in small headwater catchments with a highly dynamic stream extent. We use the resulting predictive model to generate high-frequency (∼ weekly) maps of wetted channel extent. We then identify flow thresholds from the outlet hydrograph that delineate wet and dry states across the geomorphic channel network, thus producing spatially distributed estimates of hyporheic zone flow properties at the sub-reach scale.

2 Methods

2.1 Site description

The study catchments (Dry Creek, 3.54 km^2, and Hank Creek, 5.59 km^2, the southern and northern catchments shown in Figure 1, respectively) are located within the Eel River watershed in Mendocino County, California. Average annual rainfall is approximately 1800 mm, mostly delivered during a winter wet season (typically November through April), followed by a warm dry season (May through October) (Dralle et al., 2018). Snow is rare at the site. The sites are situated within relict deep-seated earthflow terrain of the central belt melange of the Franciscan complex (Blake Jr et al., 1985; Langenheim et al., 2013), a geological assemblage made up of three roughly north-south trending belts

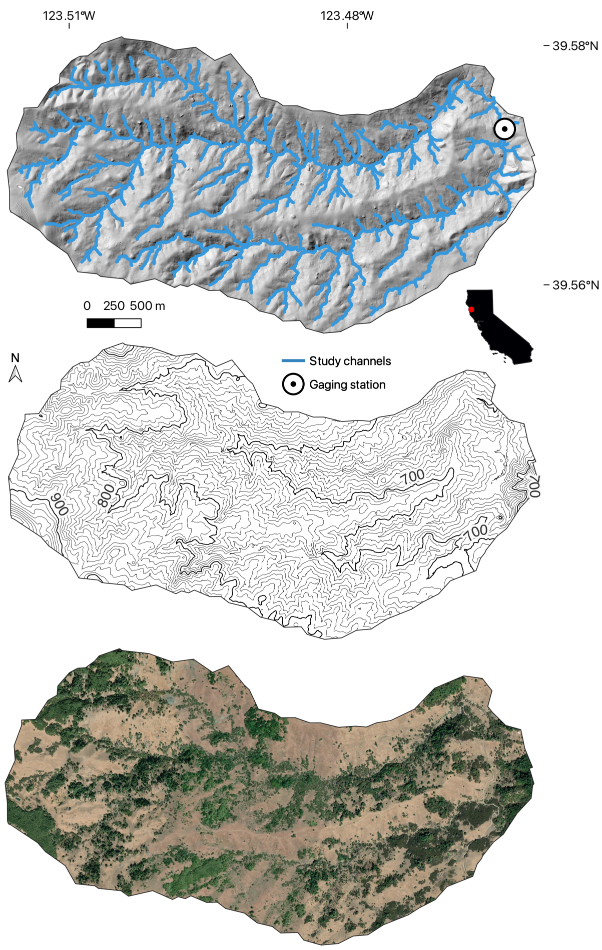

Figure 1. Hillshade of study catchments with study channels and gauging station location (top) and 10 m spaced elevation contour map (middle, elevations labeled in meters), both derived from a Lidar digital elevation model, and aerial imagery (bottom, Esri "World Imagery", accessed September 27 2022)

(coastal, central, eastern). The melange contains rocks of mixed lithology and size suspended within a clay-like, shale-derived matrix. Weathering profiles in the melange are thin, and a perennial water table can be found at depths typically less than 3 m, even at the end of the dry season (Hahm et al., 2019). In the early winter months, infiltrating rainfall rapidly replenishes root-zone water storage deficits, leading to recharge of groundwater tables that rise to the ground surface, typically within 200 mm of seasonal total rainfall (Dralle et al., 2018). Once water tables intersect the ground surface, saturation overland flow is widespread and channel networks rapidly expand, with flows that can exceed 50 mm per day (Lapides et al., 2022). Rapid flow increases are followed by comparably fast flow recessions with attendant contraction of wetted channel extent. Runoff responds rapidly to precipitation (typical lag-to-peaks in Dry and Hank Creeks of only 2-3 hrs (Lapides et al., 2022)). At runoff rates $>$ 10 mm/day, most of the geomorphic channel network has flowing water and saturation overland flow extends up adjacent hillslopes (Lapides et al., 2022). Thin weathering profiles with small water storage capacity also impact the site's plant community — a relatively sparse oak savanna, comprised of non-native annual grasses and Oregon white oak (*Quercus garryanna*) (Hahm et al., 2017, 2018, 2019).

The geomorphic channel drainage density is 16.9 km/km^2, with an average upslope contributing area at the channel heads of 1,085 m^2 (Lovill et al., 2018). Wetted channel widths at Dry and Hank Creeks vary from zero (at the geomorphic channel heads) to typical winter storm values of 5 m (for Dry) and 8 m (for Hank) at the staff gauge locations near their outlets. The upper portions of the channel network (between contributing areas of 1085 m^2 and 10,000 m^2) have very narrow channels (generally less than 1 m width), and their wetted dynamics are not considered in this study. For drainage areas above 10,000 m^2, a single power law relationship describes the geomorphic channel slope as a function of drainage area in both the Dry and Hank Creek networks (data from Lovill et al. (2018)):

$$S = 0.014A^{-0.58} \tag{1}$$

where S is channel slope (m/m) and A is drainage area (km^2). Average hillslope gradients (calculated from 1 m pixels, see below) are 28%, and landscape-wide cosmogenic nuclide-inferred erosion rates are between 0.12-0.16 mm/yr (Hahm et al., 2019).

2.2 Data sources

2.2.1 Streamflow

Streamflow data near the outlet of Dry Creek (near gaging station; Figure 1) are collected as part of the Eel River Critical Zone Observatory at a sampling frequency of 15 minutes (details in Hahm et al. (2019)). Discharge measurements were also made in Hank Creek between 2015 - 2019 (n=24, data not shown) which established that Dry and Hank Creek have nearly identical instantaneous unit runoff (discharge normalized by catchment area), leading to the use of Dry Creek's runoff (calculated with a more frequently updated rating curve) as a proxy for runoff at Hank Creek.

2.2.2 Topography

A bare earth digital elevation model (DEM) at 1 m resolution was generated from LIDAR data collected by the National Center for Airborne Laser Mapping (NCALM) in 2015 (https://doi.org/10.5069/G9WH2N2P). Geomorphic channel networks and upstream contributing areas were mapped from this DEM, which also served as the basemap for wetted channel mapping.

2.2.3 *Wetted channel extents*

Table 1. Survey dates and associated RapidEye imagery. LOO Accuracy column reports leave-one-out random forest model accuracy on training data in each row when model is trained on all training data except that described in the row or directly inferred from data in that row.

Survey date	Imagery date	Scenes	Wetted channel drainage density [km/km^2]	Q [mm/day]	Mapping method	Notes	LOO Accuracy
5/26 - 5/31/2015	6/4/2015	1	14	N/A	Walking	Early dry season (Survey 1)	77%
8/20 - 8/24/2015	8/22/2015	1	4	N/A	Walking	Late dry season (Survey 2)	84%
2/4/2018	2/12/2018	1	N/A	5	Drone	Imagery used only for points with accumulated area < 20,000 m^2, which are dry. Full drainage density unknown.	54%
N/A	3/7/2016	1	78	44	High-flow	Inferred fully wetted network based on prior wetted surveys and stream discharge	60%
N/A	6/4-8/22/2015	4	N/A	N/A	Survey 2 wet interpolation	Interpolation of wet reaches from Survey 2	8%
N/A	6/4-8/22/2015	4	N/A	N/A	Survey 1 dry interpolation	Interpolation of dry reaches from Survey 1	93%
N/A	3/15-5/26/2015	1	N/A	N/A	Survey 1 wet extrapolation	Extrapolation of wet reaches from Survey 1	66%
N/A	All July-October imagery	22	N/A	multiple	Survey 2 dry extrapolation	Extrapolation of dry reaches from Survey 2	78%
N/A	Dates when Elder Creek streamflow $\geq$0.9 mm/day	29	N/A	multiple	High-flow extrapolation	Extrapolation of wet reaches from Survey 1	19%

Data on wetted channel extents is derived or inferred from four distinct maps, which include two dry season surveys (negligible runoff) and two wet season surveys (high and low runoff) that are mapped in the left column of Figure 3. Training data are summarized in Table 1 and described in detail as follows:

Walking surveys Two boots-on-the ground walking surveys of the entirety of the Hank and Dry channel networks were performed by Lovill et al. (2018) in 2015.

Drone survey During a wet-season dry spell in February of 2018, an unmanned aerial vehicle (UAV) survey on February 4, 2018 (8 days after the most recent rainfall) revealed that channels with contributing area less than 20,000 m^2 were entirely dry. Imagery from the nearest following image date (February 12, 2018 with intervening rainfall of only about 1 mm) therefore provides "dry" observations of smaller channels (between contributing areas of 10,000 m^2 and 20,000 m^2) during the typical wet season months. This is important for training the random forest model, as it helps disentangle spectral signatures that might correlate with large extent of wetted channel (e.g. high greenness from grasses) from true spectral indicators of channel wetness.

High flow survey We identified one cloud-free image that coincides with a very high-flow rate of 34 mm/day. Field visits indicate that the channel network considered here is fully wetted at flow rates exceeding 10 mm/day (Lapides et al., 2022).

Extrapolative/interpolative surveys Machine learning approaches can require significant amounts of data for training and validation. To increase the amount of imagery data available for training, we rely on two inferential approaches. The first approach, which we refer to as 'interpolative', involves interpolating between the two walking surveys. These surveys capture the summer recession so that any reaches dry at the beginning of the summer remain dry throughout the whole summer. Conversely, any reaches that are still wet at the end of the summer are wet for the duration of time between the surveys. The streamflow timeseries Dry Creek does not begin until the winter following the surveys, but the monotonicity of the recession can be confirmed from a nearby, well-correlated stream (Dralle et al., 2018). We further extend these data using an 'extrapolative' method. Knowing that there was essentially no rainfall between March 15, 2015 and the first survey date (May 26-31, 2015) and that Elder Creek streamflow was monotonically decreasing during this period, we infer that all wet reaches during the first survey were wet for the entire period from March 15-May 26. We further noted that there was essentially no rainfall during the months of July-October during the study period, so we inferred that dry reaches during the first walking survey remained dry during all summer months in the study period. Finally, given the correspondence between Elder Creek and Dry Creek, we inferred that any wet reaches during the first walking survey (5/26-5/31/2015) would also be wet on any date on which Elder Creek runoff was a factor of 3 larger than the flows observed (0.3 mm/day at Elder Creek) during the walking survey time period.

2.2.4 Satellite imagery

We acquired 217 scenes of cloud-free and snow-free RapidEye satellite imagery (5 m pixel scale) from Planet Labs (Planet team, 2017). The imagery contains five spectral bands: 440–510 nm (blue), 520–590 nm (green), 630–685 nm (red), 690–730 nm (red edge) and 760–850 nm (near IR). All imagery were visually inspected for artefacts and other visible irregularities.

2.3 Random forest model

We trained a random forest machine learning classification model (Belgiu & Drăguţ, 2016) to identify wetted channel reaches from the satellite imagery, implemented in Python via the Scikit-Learn package (Pedregosa et al., 2011). Random forests are ensembles of decision trees, each of which is classified on a subset of the training data in order to reduce overfitting.

To create the datasets for the random forest modeling, we extracted equally spaced 10 m nodes along the geomorphic channel network. Survey data from Lovill et al. (2018) were extracted from polylines to nodes using a 1.5 m buffer. Labels for the drone survey and high-flow survey were applied directly to nodes based on area threshold criteria described above. Extrapolated and interpolated data used extracted points from other survey dates. To improve the signal-to-noise ratio of the wetted channel signal, the channel network nodes were clipped to drainage areas greater than 10,000 m^2, approximately ten times larger than the average drainage area required for channel initiation. For this reason, wetted channel extents are likely an underestimate of the true extent of wetted channel at high flow values. Each node for the relevant portions of the wetted channel maps described above was assigned a 1 (wetted) or 0 (dry) target prediction label. All RapidEye pixel band values were extracted at the location of each node for each RapidEye scene for use as input features. Predictors used for the random forest model include: blue, green, red, rededge, and near infrared bands from RapidEye pixels and normalized difference water index (Gao, 1996, (NDWI);) calculated from RapidEye pixel values.

We first split all of the available data into randomly selected training (75% of the data) and testing (25% of the data) groups. The random forest was trained on the training data group initially, and predictions were made for the test data group in order to compute accuracy metrics. We also tested the importance of each type of training data by performing leave-one-out accuracy tests for data from each row of Table 1 and any other rows based on data from that row. The entirety of the wetted channel dataset was then used to train a final classifier that was used to predict wetness states for each RapidEye image in the collection. Default Scikit-learn v1.0.1 Random Forest Classifier parameters were used: 100 trees in the forest, Gini impurity to measure the quality of splits, no maximum tree depth, two samples required per split, one minimum sample in each leaf, and the square root of the number of features considered for each split.

2.4 Power law model to relate runoff and wetted channel length

With 217 RapidEye scenes, our wetted channel maps cover a large range of conditions, but the distribution of flows on dates for which we have RapidEye scenes is not the same as the full natural distribution (see Figure 7c), due largely to the fact that clouds are more common in the wet season at higher flows. To interpolate across all possible network states, Godsey & Kirchner (2014) demonstrated that a power-law relationship may be appropriate to relate runoff at the outlet to wetted channel length. We fitted a power law curve of the form:

$$L = \alpha Q^{\beta}, \tag{2}$$

where L [$\cdot$] is the wetted channel length as a fraction of the maximum observed wetted channel length (also plotted in length units in Figure 4b), α is a positive constant, Q (mm/day) is runoff at the outlet, and $0 \leq \beta \leq 1$. We used this relationship with the full distribution of daily streamflow during the study period to infer the full distribution of wetted channel extents. We nevertheless recognize this may be an underestimate of the full extent of wetted channel at high flow values, where surface flow may extend below the 10,000 m^2 contributing area threshold used to identify study reaches.

2.5 Logistic regression model to estimate hyporheic flow capacity

Water appears at the surface when flow to a point exceeds the capacity of the subsurface to transport that flow (Hewlett & Hibbert, 1967; Godsey & Kirchner, 2014), so the flow rate at which a node transitions from dry to wet equals the subsurface flow capacity of the hyporheic zone at that point (Godsey & Kirchner, 2014; Prancevic & Kirchner, 2019; Durighetto & Botter, 2022). We fit logistic regression models to the random forest predictions of wet vs. dry as a function of instantaneous runoff at each node separately and estimated this flow capacity (ρ, in mm/day) at each node as the value at which the logistic function first predicts the reach is wetted. Since predictions at nodes were not evenly distributed between wet and dry at nodes, we weighted predictors in the logistic regression by the inverse sizes of dry and wet sample sets to ensure each sample has equal influence on the fit. Hyporheic capacity as a discharge in m^3/day ($\mathcal{P}$) was estimated by multiplying the ρ by drainage area at each node. Total cross-sectional area-integrated hyporheic transmissivity was calculated by dividing the hyporheic flow capacity in volumetric discharge units by channel slope at each node.

The logistic regression model can also be used to extend random forest predictions to all dates with runoff observations. To accomplish this, we used the estimated flow capacity at each point to determine how many nodes were wetted at each daily streamflow value during the study period. That is, where the ρ value calculated from the logistic regression is less than daily runoff, the channel is assumed to be wet on that day. The sum of wetted nodes multiplied by the node length (10 m) yields the wetted channel extent.

2.6 Hyporheic exchange flows

Longitudinal (along-stream) gradients in flow capacity estimated from the logistic regression approach may also be used to constrain hyporheic exchange flows throughout the network. We follow the model for wetted channel expansion/contraction developed by Ward et al. (2018), who posit two laterally homogeneous, parallel domains representing the surface stream environment and subsurface hyporheic zone. Surface flow only occurs where runoff exceeds down-valley flow capacity (ρ); at these places in the subsurface hyporheic zone, the continuity equation requires:

$$q_{hef} = q_{gw} - \frac{\partial \mathcal{P}}{\partial x}, \tag{3}$$

where x is defined as positive in the down-valley direction, q_{gw} is the per-channel-length contribution of groundwater (units of m^2/day), $\mathcal{P}$ is the hyporheic flow capacity expressed in volumetric flow units (m^3/day) obtained by multiplying ρ at a point by upslope contributing area at that point ($\mathcal{P} = \rho \cdot A$), and q_{hef} (m^2/day) is the channel-specific hyporheic exchange flow. Ignoring q_{gw}, Equation 3 states that if volumetric flow capacity decreases in the downstream direction (i.e. $\frac{\partial \mathcal{P}}{\partial x} < 0$), there must be exfiltration ($q_{hef} > 0$) of water from the hyporheic zone into the surface environment. Conversely, where flow capacity increases in the downstream direction ($\frac{\partial \mathcal{P}}{\partial x} > 0$), water must infiltrate into the hyporheic zone ($q_{hef} < 0$). Thus at any point in the network where flow exceeds capacity, spatial gradients in flow capacity dictate whether surface flows are infiltrating or exfiltrating from the hyporheic zone.

Numerous definitions have been proposed to quantify hyporheic exchange flows (Kasahara & Wondzell, 2003; Wondzell, 2011). Here, we calculate the average (D_{hef} m^3/day) of the magnitudes of total network-integrated exfiltrating (D_{exf}, m^3/day) and infiltrating (D_{inf}) exchange flows, and report the ratio of D_{hef} to total volumetric discharge in the stream at the outlet (D, m^3/day) across a range of flow values (D_{hef} will change with D because wetted extent, and thus the integration domain for exchange flows, changes with D). To place a lower bound on these exchange fluxes, we note that where flow capacity increases in the downstream direction (i.e. hyporheic infiltration is possible), the additional flow capacity may entirely be occupied by incoming groundwater fluxes, q_{gw}. Therefore, a lower bound on hyporheic infiltration (q_{inf}) may be calculated as:

$$q_{inf} = \max\left[0, \frac{\partial \mathcal{P}}{\partial x} - q_{gw}\right] \quad \text{where} : \frac{\partial \mathcal{P}}{\partial x} > 0. \tag{4}$$

To calculate q_{gw} along each 10 m reach between prediction points, we follow Schmadel et al. (2017) and multiply unit runoff (Q) by the contributing area difference between points, then divide by 10 m, thus obtaining a channel-length specific groundwater efflux in units of m^2/day. Where $\frac{\partial \mathcal{P}}{\partial x} < 0$, decreasing flow capacity requires that a minimum of $\frac{\partial \mathcal{P}}{\partial x}$ must exfiltrate from water stored in the hyporheic zone, in addition to exfiltra-

Variable	Dimensions	Description
L	(-)	Wetted channel drainage density (sum of length of wetted reaches normalized by total channel length)
A	L^2	Drainage area
A_0	L^2	Drainage area at outlet
D	L^3T^{-1}	Discharge at the outlet
D_{exf}	L^3T^{-1}	Exfiltration exchange flux from hyporheic zone to stream integrated across wetted channel network
D_{hef}	L^3T^{-1}	Exchange flux between stream and hyporheic zone integrated across wetted channel network; calculated as $(D_{exf} + D_{inf})/2$
D_{inf}	L^3T^{-1}	Infiltration exchange flux from stream to hyporheic zone integrated across wetted channel network
H	L	Average local reach hyporheic zone thickness
$\mathcal{P}$	$L^3\ T^{-1}$	Reach hyporheic flow capacity, expressed as volume per time
K	$L\ T^{-1}$	Average local reach flow-parallel hydraulic conductivity
q_{gw}	L^2T^{-1}	Along-reach specific groundwater inflow
q_{hef}	L^2T^{-1}	Along-reach specific exchange flux between stream and hyporheic zone
Q	$L\ T^{-1}$	Upstream-area normalized discharge (i.e., runoff) at the outlet (D/A_0)
S	(-)	Local reach slope
W	L	Average local reach hyporheic zone width
x	L	Along-reach (longitudinal) channel coordinate
α	$(TL^{-1})^{\beta}$	Scaling intercept for L-Q relationship.
β	(-)	Scaling exponent for L-Q relationship. Fraction by which L changes for a change in Q.
ρ	$L\ T^{-1}$	Reach hyporheic flow capacity, expressed as volume per time normalized by upstream area

Table 2. Description of variables

tion driven by q_{gw} (which, we note may be the groundwater itself, or exfiltrating hyporheic storage displaced by incoming groundwater). Thus, a lower bound on exfiltration of hyporheic storage is:

$$q_{exf} = -\frac{\partial \mathcal{P}}{\partial x} \quad \text{where} : \frac{\partial \mathcal{P}}{\partial x} < 0. \tag{5}$$

We integrate these length-specific rates of discharge along all wetted channel paths (i.e. where $q > \rho$), obtaining volumetric rates of infiltration (D_{inf}) and exfiltration (D_{exf}) from the hyporheic zone. Finally, following Wondzell (2011), we calculate D_{hef} as the average of these two rates:

$$D_{hef} = (D_{inf} + D_{exf})/2 \tag{6}$$

The ratio we report (D_{hef}:D) is somewhat different from Wondzell (2011), who compute D_{hef} as the channel-length specific flux (and thus their ratio has units of m^{-1}). Here, (D_{hef}:D) is dimensionless, and can be interpreted as the ratio of the average gross volumetric flux between the hyporheic zone and the stream environment (D_{hef}) to the total volumetric flux exiting the watershed (D).

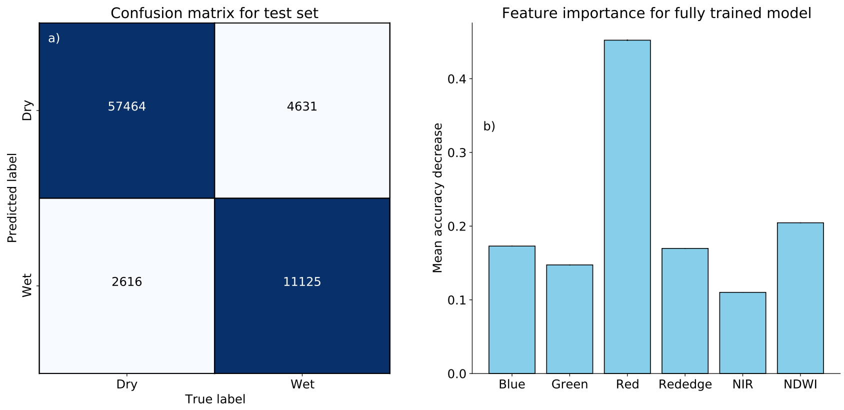

Figure 2. (a) Confusion matrix illustrating prediction accuracy of random forest classifier model (trained on 75 % of original data) on test data (25% with-held data points). (b) Permutation feature importance for features in model trained on full training data set.

3 Results

3.1 Random forest performance

Overall accuracy of the random forest model in validation is 91%. The confusion matrix in Figure 2a illustrates how this error is partitioned among false positives (channel is classified as wet when it is actually dry, lower left corner) and false negatives (channel is classified as dry when it is actually wet, upper right corner). The dark-colored diagonal of the confusion matrix contains the total number of correct classifications. In general, false negatives (predicted dry when actually wet) are much more common than false negatives. The relative prevalence of false negatives is also apparent in Figure 3g,h,i, where many wet channels are classified as dry (dark blue in subplot i). Even in this 100% wet training sample, though, prediction accuracy is quite good; 94% are predicted to be wet. The remaining rows in Figure 3 depict predictions and prediction error across other illustrative training data dates. The first two rows (a - c and d - f) illustrate predictions on the two walking survey dates from Lovill et al. (2018). The bottom row (j-l) illustrates prediction accuracy during the single drone survey date from a wet time of year (February is a peak wet season month) with channels between contributing areas of 10,000 m^2 and 20,000 m^2 that are nevertheless dry.

The leave-one-out error analysis (last column of Table 1) indicates that wet training data from different times of year are extremely important for training an accurate random forest predictor. Including the single high-flow date was not adequate to train the model to recognize wetted reaches in general. Wet training data during the dry season (fifth row of Table 1) and high-flow dates (last row of Table 1) have by far the lowest leave-one-out accuracies at 8% and 19%.

In the data supplement, we include additional analysis of the random forest model output and accuracy/uncertainty metrics. For example, we report on the agreement of trees within the random forest at different times of year under different conditions, demonstrating that inter-tree agreement is generally highest during the dry season (that is, prediction confidence is highest), and lowest from the end of the dry season through the wet season and for wet predictions in general.

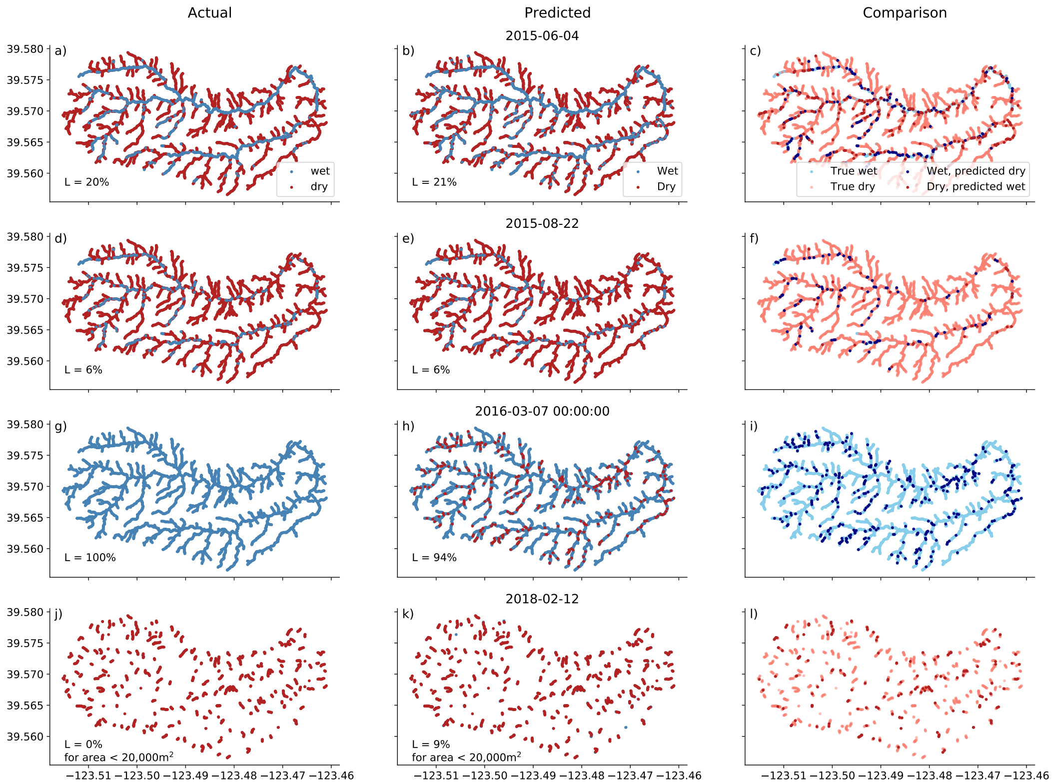

Figure 3. Visual representation of model performance on the four primary training dates. The top two rows are the surveyed dates in summer 2015. The second to third row represents a fully wetted network during a wet season peak flow event, and the bottom (drone survey data) represents an image during the wet season when many channels are nevertheless dry.

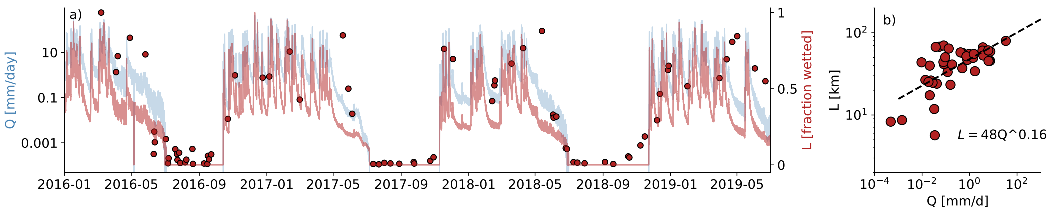

Figure 4. (a) Timeseries of Dry Creek runoff (blue) shown with timeseries of wetted channel length (red, normalized by the maximum predicted length). Scatter points are calculated from random forest modeled predictions from RapidEye satellite imagery. (b) shows the predicted wetted channel extent length as a function of outlet runoff (the power law fit excludes zero flow predictions). The continuous wetted channel prediction (red line in (a)), is estimated from the power law fit in panel (b) using the continuous streamflow timeseries.

3.2 Wetted channel dynamics and scaling

Wetted network extents predicted by the random forest (red points in Figure 4a) have seasonal patterns showing a mostly dry network in the summer when streamflow (light blue curve) is low, and variable extent during the wet season when flow varies over a few orders of magnitude (from 0.01 mm/day to nearly 50 mm/day). Consistent with theoretical expectations (Godsey & Kirchner, 2014; Prancevic & Kirchner, 2019), wetted extent generally exhibits power law scaling with runoff (Figure 4b), with a power law exponent $\beta = 0.16$. This exponent is likely an underestimate, as we do not predict wetted extent below contributing areas of 10,000 m^2, despite the fact that the network occasionally expands beyond this threshold during high flow periods (Lapides et al., 2022). The power law fit is also used to extrapolate wetted extent in Figure 4a (light red curve).

3.3 Estimates of hyporheic flow capacity

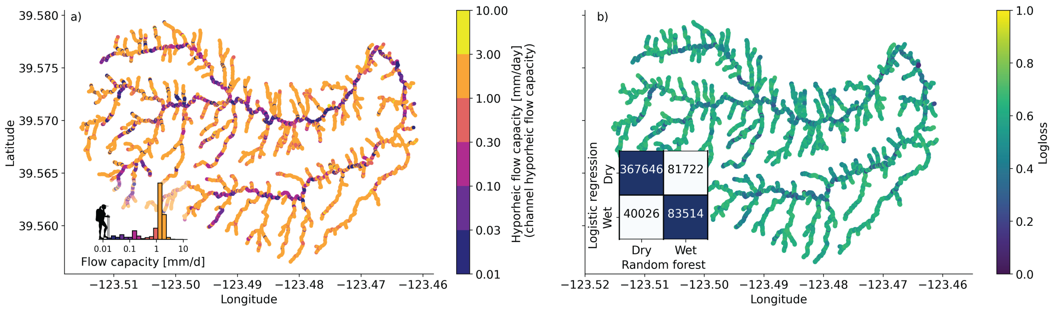

Figure 5. (a) Map of inferred hyporheic flow capacity shows decreased area-normalized (L T^{-1} units) flow capacity at higher drainage areas (main channel stems). Inset shows histogram of flow capacities. Logistic regression of flow presence versus runoff is used to calculate flow capacity (see Methods). (b) Fit quality information for flow capacity logistic regressions, including a map of log loss and (inset) a confusing matrix of logistic regression predictions compared to the random forest predictions to which they are fit. Fit quality is lower at higher logloss.

For each point throughout the network, logistic regression of the random forest predictions (wet or dry) onto runoff provides an estimate of hyporheic flow capacity (in runoff

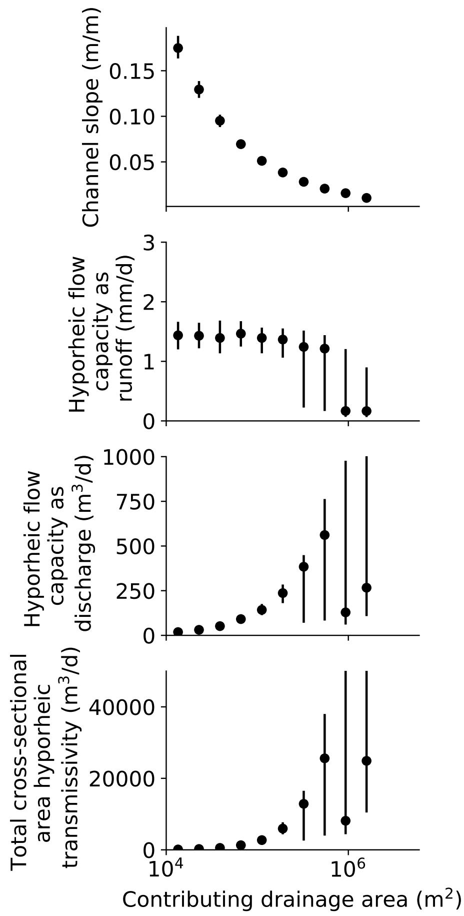

Figure 6. Network hydraulic scaling relationships: With increasing upstream contributing area, (a) channel slope decreases, (b) hyporheic flow capacity expressed as runoff (ρ) decreases, (c) hyporheic flow capacity expressed as discharge ($\mathcal{P}$) increases but then drops at high contributing areas, and (d) cross-sectional area transmissivity follows a similar increasing then decreasing pattern. Points and error bars show bin medians and the interquartile range.

units), which we map in Figure 5a (inset illustrates the probability distribution function (PDF) of flow capacities throughout the network, expressed in runoff units). Figure 5b illustrates goodness of fit of the logistic regression, expressed as logloss in the map, and via a confusion matrix in the inset. The confusion matrix illustrates whether the regression properly classifies channel wetness state under different flow conditions. As represented by logloss, fits are fair with better performance in larger channels.

When the hyporheic zone is saturated, the subsurface volumetric flow conveyed along a reach is equal to the volumetric hyporheic flow capacity $\mathcal{P} = \rho{\cdot}A$ (as above, expressed in volumetric discharge units, obtained by multiplying ρ by A, the upstream contributing area at a point). Darcy's law clarifies the channel geometry and material property controls on this flow rate:

$$\mathcal{P} = \rho \cdot A = -KHWS, \tag{7}$$

where K [L T^{-1}] is the average flow-parallel saturated hydraulic conductivity of the hyporheic zone, H is the average hyporheic cross-sectional thickness (KH is commonly described as transmissivity), W is the average hyporheic cross-sectional width, and S is the local down-reach channel slope, which serves as an approximation of the hydraulic head gradient.

Generally, flow capacities expressed as runoff units are lowest in mainstem channels (larger areas in Figure 6b, and lower values in Figure 5a inset PDF, typically between 0.01 mm/day and 1 mm/day) and highest in smaller tributaries (peak in the inset PDF between 1 and 10 mm/day), consistent with the expectation that the wetted network expands toward channel heads with increasing runoff at the outlet. Clear multimodality of the runoff flow capacity PDF (inset of Figure 5a) suggests that activation of channels is punctuated at different flow levels, with a large increase in channel length occurring near 1 mm/day when side channels activate. However, when expressed as absolute hyporheic flow capacity (discharge units), flow capacity increases with increasing drainage area, before becoming highly variable (with a smaller median value) in the main stem (Figure 6c).

3.4 L-Q relations and the persistence of wetted channel extent

Random forest prediction on imagery dates, the power law L-Q fit in Figure 4b, and the logistic regression provide three ways to explore the relationship between L and Q. We illustrate these relationships in Figure 7b, which shows that the logit and power law inferred L-Q relations fall in the point cloud of extents predicted with the random forest, although the functional forms are quite different. The logit predicts a sudden increase in wetted channel length between 1 and 2 mm/day, primarily due to expansion of the network out of the mainstem into side channels. These different methods of exploring L-Q relationships result in different probability distributions for L, plotted as cumulative distribution functions (CDFs) in Figure 7a. Differences arise because cloud-free imagery may be more readily available during dry periods, which would bias distributions inferred from imagery dates alone toward smaller wetted channel extents. This is made clear in Figure 7a, in which the CDF inferred from random forest imagery dates falls below the extents predicted from the logit and power law (which produce extent predictions on all days of the year solely as a function of discharge). Observational bias in the imagery toward dry dates is also apparent in Figure 7d, where the flow CDF predicts a higher likelihood of low flows when computed only using days on which imagery is available.

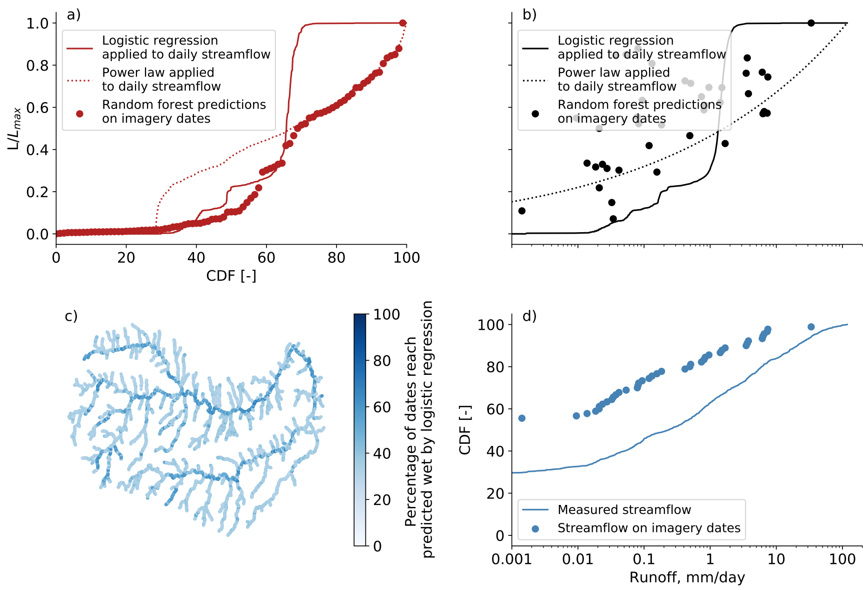

Figure 7. (a) Empirical CDF of wetted channel length from three methods: random forest-estimated wetted network length on imagery dates (scatter points), power law model trained on random forest results aggregated to total network length applied to all daily streamflow (dotted line), and logistic regression trained at each reach on random forest results applied to all daily streamflow (solid line). (b) Relationship between runoff and wetted channel length as estimated by each of the three methods. (c) Map of reach persistence based on logistic regression applied to all daily streamflow. (d) CDF of runoff using (solid line) all streamflow data during the study period and (scatter points) only streamflow on imagery dates.

3.5 Hyporheic exchange flows

Figure 8 plots the hyporheic exchange flux (D_{hef}) relative to volumetric discharge at the outlet (D) across a range of flow exceedance probabilities. The colorbar plots the correspondence between exceedance probability and runoff. For small exceedances (large flows), hyporheic exchange fluxes are comparable in magnitude to outlet discharge (D_{hef}:D ≈ 1), whereas at low flows, the exchange flux magnitude increases to > 100 times discharge at the outlet.

4 Discussion

4.1 Surface water presence detection in small headwater stream networks

The simplest, but perhaps most important, potential application of this work is to aide ecological monitoring of channel networks. As hydrological regimes shift in response to increasing anthropogenic pressures and a changing climate, so too will the wetted extent of channel networks (Lapides et al., 2021), with consequences for food webs, sedimentation, riverine nutrient cycling, habitat extent/quality, and other ecological processes (Bernal et al., 2004; Hwan & Carlson, 2016; Sabo et al., 2010; Larned et al., 2010; Arthington et al., 2005). A remote-sensing based framework for detecting the absence

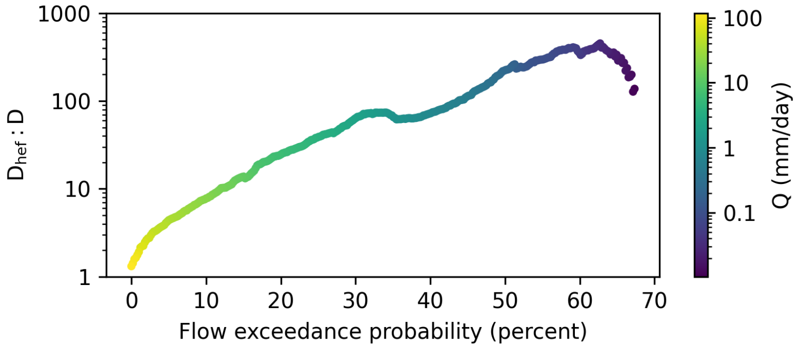

Figure 8. Magnitude of inferred, network-integrated hyporheic exchange flows relative to volumetric discharge at the catchment outlet across a range of flow values (expressed as runoff (mm/day) and as a flow exceedance probability).

or presence of water in (often difficult-to-access) headwater stream networks would contribute to ongoing efforts to address this significant challenge in watershed management (Moidu et al., 2021).

4.2 Hyporheic flow properties across river networks

Drivers of surface water presence throughout headwater stream networks include: upstream runoff production, hyporheic zone transmissivity (hydraulic conductivity times average conductive depth), channel width, and slope (Ward et al., 2018). Channel slope can be approximated across landscapes using DEMs. However, both the spatial pattern of width-integrated transmissivity and the variation in runoff production are poorly constrained by our current datasets and understanding (Thompson et al., 2011; Prancevic & Kirchner, 2019). Timeseries of wetted channel extent reflect the spatial patterns in both of these fundamental but difficult-to-measure hydrological variables. Given an assumption about the pattern of transmissivity (such as the scaling relationship proposed in Prancevic & Kirchner, 2019), runoff production can be inferred from wetted channel maps. Conversely, given the assumption of spatial uniformity of runoff (Durighetto & Botter, 2022), the pattern of transmissivity (and thus hyporheic zone flow capacity, ρ) can be inferred. The latter assumption is applied in this work to map ρ throughout the Dry and Hank Creek channel networks.

Estimating ρ using the presented method requires high spatio-temporal resolution observations of wetted channel extent, but avoids unnecessary assumptions about the contributing-area scaling of hyporheic zone properties, thus generalizing the functional relationship (Figure 7b) between wetted channel length and discharge (Durighetto & Botter, 2022). The approach can account for the often discrete and discontinuous properties inherent in the geomorphology and geometry of channel networks. For example an abrupt transition from a pool to a riffle, or from a tributary to a mainstem channel, might be accompanied by a large change in ρ (Käser et al., 2009; Schmadel et al., 2017). Here, the method revealed punctuated activation of different channels (mainstem versus side channels) that resulted in a stepped L versus Q relationship (Figure 7b), which cannot be captured by the power-law L-Q model that emerges from presumed scaling relationships between contributing area and hyporheic zone transmissivity (Prancevic & Kirchner, 2019).

Estimates of ρ may also be useful in surface-groundwater exchange models, where parameters representing subsurface properties can influence understanding of hyporheic zone processes (Schmadel et al., 2017). In Figure 8, we used distributed ρ estimates to calculate that the magnitude of exchange fluxes relative to discharge ($D_{hef} : D$) increases significantly as flows decline, supporting the expectation that the influence of hyporheic processes on water quality (e.g. temperature, chemistry) is greater at low flows (Wondzell, 2011). Estimates of ρ could straightforwardly be used to parameterize subsurface elements of spatially distributed hyporheic zone models (e.g. Ward et al., 2018).

4.3 Challenges and opportunities

We introduced a generic workflow that nevertheless remains untested in different environments. Perhaps most obvious is the need to try the approach in more heavily forested watersheds where the channel may not be so easily observed with satellite imagery. Even in such forested watersheds, higher resolution remote sensing data products with different sensing capabilities (e.g. Satellite Vu, `https://www.satellitevu.com/`) and rapidly advancing unmanned aerial systems may make it possible to capture glimpses of channels through thick canopy.

Another limitation of the method is the availability of training data. Machine learning approaches are data hungry, and the leave-one-out exercise in Table 1 reveals the relative importance of different training data in our seasonal watershed. However, we developed reasonable heuristics to increase the size of a training dataset in data sparse environments, or where channel surveys are infrequent. For example, if a reach is mapped as dry for $q = q_0$, it stands to reason that reach will remain dry for $q = q_1 << q_0$, making it possible to utilize imagery on various dates for training a machine learning model. Analogously, if a reach is mapped as wet for $q = q_0$, it likely remains wet for $q = q_2 >> q_0$. These heuristics (which follow from the flow emergence principle and the uniform runoff assumption) make it possible to expand sparse training datasets to include a wider range of environmental and flow conditions.

Higher data availability and quality may never answer whether machine learning models, which are difficult to interpret mechanistically, are getting the right answers for the right reasons. Is our random forest model truly 'seeing' the water in the channels? There are promising indicators. The model performs very well in validation, and coherent scaling relationships between contributing area and hyporheic flow properties emerge (e.g. mainstems have demonstrably lower ρ; Figure 6). The latter is promising considering we did not use contributing area as a predictor; when contributing area is included, results are generally similar. A random forest model is also among the less sophisticated machine learning models; more complex methods (e.g. convolutional neural networks) may provide additional support for the validity of the general approach, and may in fact be necessary in more challenging settings where, for example, canopy cover obscures channels.

5 Conclusion

Wetted channel extent and stream intermittency affect the structure and function of riverine ecosystems, and are observable signatures of difficult-to-observe subsurface hydrological processes. We demonstrate a proof-of-concept approach for using hyperspectral imagery and machine learning trained on observational data to monitor the growth and contraction of a headwater stream at high spatial and temporal resolution. The method predicts water presence with 91% accuracy. Assuming unit runoff is spatially uniform, and that water emerges in the channel when up-network runoff production exceeds the flow capacity of the hyporheic zone, we use predicted maps of channel extent to estimate hyporheic hydrogeologic properties and hyporheic exchange. The approach has promising applications in environmental monitoring, and details a prototypical workflow for potential applications in other environments.

References

Allen, G. H., Pavelsky, T. M., Barefoot, E. A., Lamb, M. P., Butman, D., Tashie, A., & Gleason, C. J. (2018). Similarity of stream width distributions across headwater systems. *Nature communications*, *9*(1), 1–7.

Arthington, A. H., Balcombe, S. R., Wilson, G. A., Thoms, M. C., & Marshall, J. (2005). Spatial and temporal variation in fish-assemblage structure in isolated waterholes during the 2001 dry season of an arid-zone floodplain river, cooper creek, australia. *Marine and Freshwater Research*, *56*(1), 25–35.

Belgiu, M., & Drăguţ, L. (2016). Random forest in remote sensing: A review of applications and future directions. *ISPRS journal of photogrammetry and remote sensing*, *114*, 24–31.

Bernal, S., Butturini, A., Riera, J., Vázquez, E., & Sabater, F. (2004). Calibration of the inca model in a mediterranean forested catchment: the effect of hydrological inter-annual variability in an intermittent stream. *Hydrology and Earth System Sciences*, *8*(4), 729–741.

Beven, K. J., & Kirkby, M. J. (1979). A physically based, variable contributing area model of basin hydrology/un modèle à base physique de zone d'appel variable de l'hydrologie du bassin versant. *Hydrological sciences journal*, *24*(1), 43–69.

Bishop, K., Buffam, I., Erlandsson, M., Fölster, J., Laudon, H., Seibert, J., & Temnerud, J. (2008). Aqua Incognita: the unknown headwaters. *Hydrological Processes*, *22*(8), 1239–1242. (_eprint: https://onlinelibrary.wiley.com/doi/pdf/10.1002/hyp.7049) doi: 10.1002/hyp.7049

Blake Jr, M. C., Jayko, A., & McLaughlin, R. (1985). Tectonostratigraphic terranes of the northern coast ranges, california.

Carbonneau, P. E., Belletti, B., Micotti, M., Lastoria, B., Casaioli, M., Mariani, S., ... Bizzi, S. (2020). Uav-based training for fully fuzzy classification of sentinel-2 fluvial scenes. *Earth surface processes and landforms*, *45*(13), 3120–3140.

Chambers, J. Q., Robertson, A. L., Carneiro, V., Lima, A. J., Smith, M.-L., Plourde, L. C., & Higuchi, N. (2009). Hyperspectral remote detection of niche partitioning among canopy trees driven by blowdown gap disturbances in the central amazon. *Oecologia*, *160*(1), 107–117.

Datry, T., Larned, S. T., & Scarsbrook, M. R. (2007). Responses of hyporheic invertebrate assemblages to large-scale variation in flow permanence and surface–subsurface exchange. *Freshwater Biology*, *52*(8), 1452–1462.

Dralle, D. N., Hahm, W. J., Rempe, D. M., Karst, N. J., Thompson, S. E., & Dietrich, W. E. (2018). Quantification of the seasonal hillslope water storage that does not drive streamflow. *Hydrological Processes*, *32*(13), 1978–1992.

Dugdale, S. J., Klaus, J., & Hannah, D. M. (2022). Looking to the skies: realising the combined potential of drones and thermal infrared imagery to advance hydrological process understanding in headwaters. *Water Resources Research*, *58*(2), e2021WR031168.

Durighetto, N., & Botter, G. (2022). On the relation between active network length and catchment discharge. *Geophysical Research Letters*, *49*(14), e2022GL099500.

Durighetto, N., Vingiani, F., Bertassello, L. E., Camporese, M., & Botter, G. (2020). Intraseasonal Drainage Network Dynamics in a Headwater Catchment of the Italian Alps. *Water Resources Research*, *56*(4), e2019WR025563. doi: 10.1029/2019WR025563

Fovet, O., Belemtougri, A., Boithias, L., Braud, I., Charlier, J.-b., Cottet, M., ... others (2021). Intermittent rivers and ephemeral streams: Perspectives for critical zone science and research on socio-ecosystems. *Wiley Interdisciplinary Reviews: Water*, *8*(4), e1523.

Gao, B.-C. (1996). Ndwi—a normalized difference water index for remote sensing of vegetation liquid water from space. *Remote sensing of environment*, *58*(3), 257–266.

Godsey, S. E., & Kirchner, J. W. (2014, November). Dynamic, discontinuous stream networks: hydrologically driven variations in active drainage density, flowing channels and stream order. *Hydrological Processes*, *28*(23), 5791–5803. (00010) doi: 10.1002/hyp.10310

Hahm, W. J., Dietrich, W. E., & Dawson, T. E. (2018). Controls on the distribution and resilience of quercus garryana: ecophysiological evidence of oak's water-limitation tolerance. *Ecosphere*, *9*(5), e02218.

Hahm, W. J., Dralle, D. N., Lovill, S. M., Rose, J., Dawson, T. E., & Dietrich, W. E. (2017). *Exploratory tree survey (2016 - eel river critical zone observatory - sagehorn - central belt melange, franciscan complex, northern california coast ranges, usa).*

Hahm, W. J., Rempe, D. M., Dralle, D. N., Dawson, T. E., Lovill, S. M., Bryk, A. B., ... Dietrich, W. E. (2019). Lithologically controlled subsurface critical zone thickness and water storage capacity determine regional plant community composition. *Water Resources Research*, *55*(4), 3028–3055.

Hewlett, J. D., & Hibbert, A. R. (1967). Factors affecting the response of small watersheds to precipitation in humid areas. *Forest hydrology*, *1*, 275–290.

Hwan, J., & Carlson, S. (2016). Fragmentation of an intermittent stream during seasonal drought: Intra-annual and interannual patterns and biological consequences. *River Research and Applications*, *32*(5), 856–870.

Jaeger, K. L., Hafen, K. C., Dunham, J. B., Fritz, K. M., Kampf, S. K., Barnhart, T. B., ... others (2021). Beyond streamflow: call for a national data repository of streamflow presence for streams and rivers in the united states. *Water*, *13*(12), 1627.

Kampf, S. K., Dwire, K. A., Fairchild, M. P., Dunham, J., Snyder, C. D., Jaeger, K. L., ... others (2021). Managing nonperennial headwater streams in temperate forests of the united states. *Forest Ecology and Management*, *497*, 119523.

Kasahara, T., & Wondzell, S. M. (2003). Geomorphic controls on hyporheic exchange flow in mountain streams. *Water Resources Research*, *39*(1), SBH–3.

Käser, D. H., Binley, A., Heathwaite, A. L., & Krause, S. (2009). Spatio-temporal variations of hyporheic flow in a riffle-step-pool sequence. *Hydrological Processes: An International Journal*, *23*(15), 2138–2149.

Langenheim, V., Jachens, R. C., Wentworth, C. M., & McLaughlin, R. J. (2013). Previously unrecognized regional structure of the coastal belt of the franciscan complex, northern california, revealed by magnetic data. *Geosphere*, *9*(6), 1514–1529.

Lapides, D. A., Hahm, W. J., Rempe, D. M., Dietrich, W. E., & Dralle, D. N. (2022). Controls on stream water age in a saturation overland flow-dominated catchment. *Water Resources Research. 58 (4): e2021WR031665*, *58*(4).

Lapides, D. A., Leclerc, C. D., Moidu, H., Dralle, D. N., & Hahm, W. J. (2021). Variability of stream extents controlled by flow regime and network hydraulic scaling. *Hydrological Processes*, *35*(3), e14079.

Larned, S. T., Datry, T., Arscott, D. B., & Tockner, K. (2010). Emerging concepts in temporary-river ecology. *Freshwater Biology*, *55*(4), 717–738.

Li, D., Wu, B., Chen, B., Qin, C., Wang, Y., Zhang, Y., & Xue, Y. (2020). Open-surface river extraction based on sentinel-2 msi imagery and dem data: case study of the upper yellow river. *Remote Sensing*, *12*(17), 2737.

Ling, F., Li, X., Foody, G. M., Boyd, D., Ge, Y., Li, X., & Du, Y. (2020). Monitoring surface water area variations of reservoirs using daily modis images by exploring sub-pixel information. *ISPRS Journal of Photogrammetry and Remote Sensing*, *168*, 141–152.

Lovill, S. M., Hahm, W. J., & Dietrich, W. E. (2018). Drainage from the Critical Zone: Lithologic Controls on the Persistence and Spatial Extent of Wetted Channels during the Summer Dry Season. *Water Resources Research*, *54*(8), 5702–5726. (_eprint: https://agupubs.onlinelibrary.wiley.com/doi/pdf/10.1029/2017WR021903) doi: 10.1029/2017WR021903

Moidu, H., Obedzinski, M., Carlson, S., & Grantham, T. (2021). Spatial patterns and sensitivity of intermittent stream drying to climate variability. *Water Resources Research*, *57*(11), e2021WR030314.

Pedregosa, F., Varoquaux, G., Gramfort, A., Michel, V., Thirion, B., Grisel, O., ... Duchesnay, E. (2011). Scikit-learn: Machine learning in Python. *Journal of Machine Learning Research*, *12*, 2825–2830.

Perez-Saez, J., Mande, T., Larsen, J., Ceperley, N., & Rinaldo, A. (2017). Classification and prediction of river network ephemerality and its relevance for waterborne disease epidemiology. *Advances in Water Resources*, *110*, 263–278.

Planet application program interface: In space for life on earth. (2017). (urlhttps://api.planet.com)

Prancevic, J. P., & Kirchner, J. W. (2019). Topographic Controls on the Extension and Retraction of Flowing Streams. *Geophysical Research Letters*, *46*(4), 2084–2092. (_eprint: https://agupubs.onlinelibrary.wiley.com/doi/pdf/10.1029/2018GL081799) doi: 10.1029/2018GL081799

Qin, P., Cai, Y., & Wang, X. (2021). Small waterbody extraction with improved u-net using zhuhai-1 hyperspectral remote sensing images. *IEEE Geoscience and Remote Sensing Letters*, *19*, 1–5.

Sabo, J. L., Finlay, J. C., Kennedy, T., & Post, D. M. (2010). The role of discharge variation in scaling of drainage area and food chain length in rivers. *science*, *330*(6006), 965–967.

Schmadel, N. M., Ward, A. S., & Wondzell, S. M. (2017). Hydrologic controls on hyporheic exchange in a headwater mountain stream. *Water Resources Research*, *53*(7), 6260–6278.

Thompson, S. E., Harman, C. J., Troch, P. A., Brooks, P. D., & Sivapalan, M. (2011). Spatial scale dependence of ecohydrologically mediated water balance partitioning: A synthesis framework for catchment ecohydrology. *Water Resources Research*, *47*(10).

Verma, U., Chauhan, A., MM, M. P., & Pai, R. (2021). Deeprivwidth: Deep learning based semantic segmentation approach for river identification and width measurement in sar images of coastal karnataka. *Computers & Geosciences*, *154*, 104805.

Wang, X., Gong, J., Zhang, Y., & Atkinson, P. M. (2022). Near real-time surface water extraction from goes-16 geostationary satellite abi images by constructing and sharpening the green-like band. *Science of Remote Sensing*, 100055.

Ward, A. S., Schmadel, N. M., & Wondzell, S. M. (2018, apr). Simulation of dynamic expansion, contraction, and connectivity in a mountain stream network. *Advances in Water Resources*, *114*, 64–82. doi: 10.1016/j.advwatres.2018.01.018

Whiting, J. A., & Godsey, S. E. (2016). Discontinuous headwater stream networks with stable flowheads, Salmon River basin, Idaho. *Hydrological Processes*, *30*, 2305-2316.

Wondzell, S. M. (2011). The role of the hyporheic zone across stream networks. *Hydrological Processes*, *25*(22), 3525–3532.

Wondzell, S. M., & Ward, A. S. (2022). The channel-source hypothesis: Empirical evidence for in-channel sourcing of dissolved organic carbon to explain hysteresis in a headwater mountain stream. *Hydrological Processes*, *36*(5), e14570.

Xue, Y., Qin, C., Wu, B., Li, D., & Fu, X. (2022). Automatic extraction of mountain river surface and width based on multisource high-resolution satellite images. *Remote Sensing*, *14*(10), 2370.

Zanetti, F., Durighetto, N., Vingiani, F., & Botter, G. (2022). Analyzing river network dynamics and the active length–discharge relationship using water presence sensors. *Hydrology and Earth System Sciences*, *26*(13), 3497–3516.